Adaptive Compressed Tomography Sensing

Oren Barkan, Jonathan Weill, Amir Averbuch
School of Computer Science
Tel Aviv University
orenbarkan@post.tau.ac.il

Shai Dekel
GE Global Research

Abstract

One of the main challenges in Computed Tomography (CT) is how to balance between the amount of radiation the patient is exposed to during scan time and the quality of the CT image. We propose a mathematical model for adaptive CT acquisition whose goal is to reduce dosage levels while maintaining high image quality at the same time. The adaptive algorithm iterates between selective limited acquisition and improved reconstruction, with the goal of applying only the dose level required for sufficient image quality. The theoretical foundation of the algorithm is nonlinear Ridgelet approximation and a discrete form of Ridgelet analysis is used to compute the selective acquisition steps that best capture the image edges. We show experimental results where for the same number of line projections, the adaptive model produces higher image quality, when compared with standard limited angle, non-adaptive acquisition algorithms.

1. Introduction

In the last decade, several studies have shown that radiation exposure during CT scanning is a significant factor in raising the total public risk of cancer deaths [1,20,21]. To balance between image quality and these concerns, radiologists use the protocol: As Low as Reasonably Achievable (ALARA). It's meant to ensure that "…CT dose factors are kept to a point where risk is minimized for maximum diagnostic benefit...", where the dose can be determined by the product of the CT tube current and the time the patient is exposed to radiation (see [2] for an overview). Currently, there are several state-of-the-art technologies that attempt to achieve dose reduction. Iterative Reconstruction (IR) methods are successful in reducing artifacts, improving resolution and lowering the noise in the reconstructed images [3,4]. More recently, Model Based Iterative Reconstruction (MBIR) [6] was introduced. It improves upon the IR methods by incorporating accurate system models coupled with statistical noise models and prior models. However, dosage levels during CT exams are still at the focus of attention and any new method that can reduce them is considered highly valuable.

This paper describes an adaptive acquisition model that is superior, in the CT image quality, to existing limited angle, non-adaptive acquisition methods and in theory may allow minimal and optimal dosage levels. The method can be considered a significant generalization of existing two-step adaptive acquisition methods [7,8] and can potentially use the same hardware configurations that are capable of changing their geometric configuration and acquisition protocols on-the-fly [9].

Observe that adaptive acquisition should not be confused with adaptive reconstruction. In the latter, the acquisition model is a non-adaptive uniform sampling scheme, where over a discrete set of pre-determined angles, line projections are computed at equal intervals. In this setup, the adaptive elements, if exist, are part of the post-acquisition reconstruction step.

The outline of the algorithm is as follows: First, the system projects the object with an extreme low dose according to a uniform predetermined pattern and reconstructs an initial low quality image. Next, the system predicts from the reconstructed low quality image where the significant edges of the true objects are and projects along them. Then, the system iterates by incorporating the newly added line projections in order to obtain a refined approximation of the object's image. The algorithm continues to iterate between estimation of locations of significant features, adaptive acquisition and reconstruction until a convergence criterion is met. The goal is to converge to a high quality reconstruction using a minimal number of rays (line projections). The method relies on the mathematical model of Ridgelets [5], and therefore has a natural multiresolution capability, where the significance of edges is analyzed at different scales. The mathematical theory of [5] quantifies, in the setup of CT, the geometric 'structure' of the image and how fast a Ridgelet approximation converges to the image. Our algorithm, whose goal is to acquire an unknown image, regards the adaptive Ridgelet approximation of the image as the 'optimal' benchmark and is designed to match its performance. This approach has strong ties with the

1063-6919/13 $26.00 © 2013 IEEE
DOI 10.1109/CVPR.2013.285

waveform analysis presented in [10] that allowed the authors to classify singularities and quantify the 'stability' of limited angle tomography. Indeed, although in our work we limit the number of line projections, but do not limit the angles, the fundamental understanding of the relationship between a function's edge singularities and its Radon representation, as explained in [10], is at the core of our algorithm (see Figure 3.1 and the accompanying explanation). We show in the experimental results section that for the same number of line projections, our algorithm yields higher image reconstruction quality, when compared with known limited angle, non-adaptive acquisition algorithms.

The paper is organized as follows: Section 2 overviews necessary mathematical background. Section 3 describes in detail our adaptive acquisition algorithm. Experimental results and comparisons with non-adaptive methods are given in Section 4. In Section 5 we draw conclusions and discuss future work.

2. Preliminaries

2.1 Fast algorithms for Total Variation functionals with 'sparse' constraints

For a given image $I \in \mathbb{R}^{m\times m}$, with pixels values $\{I_{i,j}\}$, we define the gradient of I by $\nabla I_{i,j} = (I_{i,j} - I_{i-1,j}, I_{i,j} - I_{i,j-1})$. The Total Variation (TV) norm of the image is given by $|I|_{TV} \triangleq \sum_{i,j=2}^{m} \left(|I_{i,j} - I_{i-1,j}| + |I_{i,j} - I_{i,j-1}| \right)$. Denote $N = m^2$ and let $x \in \mathbb{R}^N$ be a one-dimensional representation of I by concatenating the columns of I into a single column vector $x = (I_{1,1}, I_{2,1}, \ldots, I_{m,1}, \ldots, I_{1,m}, \ldots I_{m,m})^T$. Given an $n \times N$ ($n << N$) sampling matrix $A \in \mathbb{R}^{n\times N}$ and corresponding observations vector $y \in \mathbb{R}^n$, generated by $Ax = y$, the so-called TV-minimization is concerned with solving one of the following optimization problems:

$$\min_U |U|_{TV} \quad s.t.\ Au = y \qquad (2.1)$$

$$\min_U |U|_{TV} + \mu \|Au - y\|_2^2 \qquad (2.2)$$

where $u \in \mathbb{R}^N$ is the one-dimensional representation of $U \in \mathbb{R}^{m\times m}$ and μ is a given weight parameter. The minimization problem (2.2) is applied in the presence of noise in the sampling process and the weight μ depends, in part, on the expected noise level. This model is difficult to solve directly due to non-differentiability and non-linearity of the TV term. During the last few years there has been an explosion of new numeric iterative solvers (see the papers in the "Compressive Sensing Recovery Algorithms" section of [11]).

Although conceptually our method may use such solvers as black boxes, its unique features allow us to apply critical modifications that not only accelerate the iterative methods, but also make them feasible in large datasets problems when N is large. In this work, we implemented a modified version of the TVAL3 solver [12,13]. Our modified version utilizes the fact that in our special case the matrix A is highly sparse. This is in complete contrast to the usual setup in compressed sensing, where the theory dictates a dense matrix (usually of pseudo-random nature). As we shall see in Section 3, in our case, the sparsity is due to the fact that each row of A is associated with weighted integration over a digital line in the image I and therefore a vector of weights. Each weight value corresponds to a pixel in I and determined by the amount of intersection between the analytic line and the pixel itself. As a result, only weights that are located in entries associated with the pixels of the digital line have non-zero values. Thus, each row in matrix A has $\leq cm = c\sqrt{N}$ (where $c < 2$) non-zero entries. We note that even if we use a more accurate model based interpolation, where the line is given more significant width, the matrix A would remain sparse. This structure allows us to reduce memory consumption, to adaptively update a sparse data structure for A and to implement fast linear algebra operations. This idea is not new to the CT community. Moreover, for practical clinical data sizes in 3D helical uniform acquisition, the matrix A can be too large to hold in memory and must be computed on the fly. Also, its form is carefully determined from the geometry of the focal spots and detectors [14]. In this work we focus on the 2D model and in future work we plan to investigate whether in the 3D case our smaller adaptive sampling set can be stored in memory or computed on-the-fly.

2.2 Ridgelets

Let $\psi \in L_2(\mathbb{R})$ be a wavelet [15]. A bivariate Ridgelet function [16] is defined by

$$\psi_{a,b,\theta}(x_1, x_2) \triangleq a^{-1/2} \psi((x_1 \cos\theta + x_2 \sin\theta - b)/a),$$

where a, b and θ are the parameters determining the scale, translation and rotation of the Ridgelet function, respectively.

Given $f \in L_1(\mathbb{R}^2)$, its Continuous Ridgelet Transform [16] (CRT) is defined by

$$CRT_f(a,b,\theta) \triangleq \int_{\mathbb{R}^2} \psi_{a,b,\theta}(x) f(x) dx. \qquad (2.3)$$

The continuous Radon transform [17] of a bivariate function f at direction θ is defined as

$$R_f(\theta,t) \triangleq \int_{\mathbb{R}^2} f(x_1,x_2)\delta\left(x_1\cos\theta + x_2\sin\theta - t\right)dx_1dx_2,$$

where δ is the Dirac function. The Radon and the Ridgelet transforms are related by

$$CRT_f(a,b,\theta) = \int_{\mathbb{R}} \psi_{a,b}(t) R_f\left(\theta,t\right)dt, \qquad (2.4)$$

where $\psi_{a,b}(x) \triangleq a^{-1/2}\psi((x-b)/a)$. In applications, this means that the Ridgelet transform can be computed by the application of the Radon transform at a given angle, followed by 1D fast wavelet transform [15].

We find that Ridgelets are the right mathematical tool in the setup of CT, because the acquisition device is not able to capture, through its sampling process, well localized functionals such as Curvelet coefficients. Observe that in the context of CT reconstruction, Curvelets have been used as a regularization tool [23].

From approximation theoretical perspective, the mathematical foundation of our adaptive algorithm follows the framework of characterizing the images by the appropriate function smoothness spaces and then providing an estimate for the order of convergence.

Definition 2.1 [5]: For $\alpha > 0$, and $p,q > 0$, we say that $f \in \dot{R}^{\alpha}_{p,q}\left(\mathbb{R}^2\right)$, if $f \in L_1\left(\mathbb{R}^2\right)$ and

$$\|f\|_{\dot{R}^{\alpha}_{p,q}} \triangleq \left(\sum_{j=-\infty}^{\infty} 2^{j(\alpha+1/2)q}\left(\frac{1}{\pi}\int_0^{\pi}\left\|CRT_f\left(2^j,\cdot,\theta\right)\right\|_p^p d\theta\right)^{q/p}\right)^{1/q} < \infty.$$

We note that this definition requires certain conditions on the wavelet ψ, such as sufficient vanishing moments (with respect to α) and its decay, which we shall omit here. These conditions ensure that membership in the smoothness space $\dot{R}^{\alpha}_{p,q}$ does not depend on the particular wavelet used in (2.3). In this work we assume that the functions we analyze are compactly supported in a 'standard' compact domain such as $\left[-1,1\right]^2$ and attain the value zero on its boundary. Indeed, CT images satisfy this requirement (see the examples below). Therefore, by a simple zero extension argument, a function $f \in L_2\left(\left[-1,1\right]^2\right)$ of this nature can also be regarded as a function in $L_1\left(\mathbb{R}^2\right)\bigcap L_2\left(\mathbb{R}^2\right)$. By sampling the CRT, one may obtain a discrete Ridgelet Frame system $\left\{\psi_{\gamma}\right\}$ with a dual system $\left\{\tilde{\psi}_{\gamma}\right\}$, for a countable index $\left\{\gamma = (a,b,\theta)\right\}$, such that for $f \in L_2\left(\left[-1,1\right]^2\right)$, $f = \sum_{\gamma}\left\langle f,\tilde{\psi}_{\gamma}\right\rangle\psi_{\gamma} = \sum_{\gamma}\left\langle f,\psi_{\gamma}\right\rangle\tilde{\psi}_{\gamma}$.

Recall, that the frame property guarantees 'stability' of the representation, in the sense that there exist constants $0 < A \le B < \infty$, such that

$$A\|f\|_2^2 \le \sum_{\gamma}\left|\left\langle f,\psi_{\gamma}\right\rangle\right|^2 \le B\|f\|_2^2, \quad \forall f \in L_2\left(\left[-1,1\right]^2\right).$$

Let us rearrange the Ridgelet coefficients based on the size of their absolute values $\left|\left\langle f,\psi_{\gamma_1}\right\rangle\right| \ge \left|\left\langle f,\psi_{\gamma_2}\right\rangle\right| \ge \cdots$, and denote the n-term adaptive approximation to f by $f_n \triangleq \sum_{i=1}^{n}\left\langle f,\psi_{\gamma_i}\right\rangle\tilde{\psi}_{\gamma_i}$. Then, we have the Jackson-type estimate [5] for $\alpha > 1/2$ and $1/\tau = \alpha - 1/2$, $\left\|f - f_n\right\|_{L_2\left(\left[-1,1\right]^2\right)} \le cn^{-\alpha/2}\left\|f\right\|_{\dot{R}^{\alpha}_{\tau,\tau}}$. Thus, under certain assumptions on the input function, not only the convergence of the adaptive approximation is ensured, but its rate is also estimated. The outcome the theory is that the approximation rate of an adaptive Ridgelet approximation depends on the smoothness of the function in a given Ridgelet smoothness space.

As we shall see in Section 3, our adaptive acquisition method follows the adaptive Ridgelet approximation to the image I as a model. It tries to predict from iterative approximation to I, the significant Ridgelet coefficients. Then we use these coefficients in order to select the next set of line projections that are considered as best candidates to project I with, in the subsequent iteration.

3. Adaptive Tomography Acquisition (ATA)

Before presenting the details of the ATA algorithm, we first provide an instructive and useful example: Assume we had an access to an optimal 'oracle'. We then ask, how many line projections are needed as rows in the matrix A, such that the image of Figure 3.1(a) can be reconstructed with high precision, by solving (2.1) ?

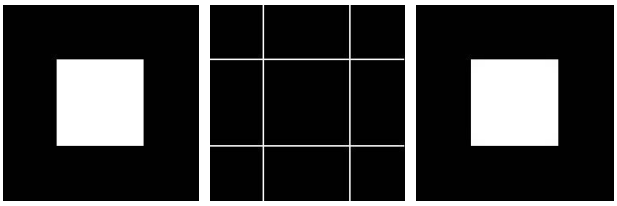

(a) Original image (b) Sampled 8 line Projections (c) Reconstruction, perfect (PSNR= ∞)

Figure 3.1: Reconstruction of 'Square' image of size 256x256

The surprising result is that, equipped with an 'oracle', this image can be reconstructed with perfect precision, where the matrix A in (2.1) contains only 8 rows associated with 8 line projections. Thus, the numbers of samples satisfies $n = 0.000122N$, which is a tiny fraction of the size of the image, $N = 256\times 256$. This is achieved by selecting the unique four pairs of line projections that

are the immediate neighbors of each of the four lines associated with the edges of the white square. Figs 3.1(b) and (c) show the locations of the line projections and the reconstructed image, respectively.

The moral of this example, which correlates well with the theory in [5], is that during the acquisition process, we should try to adaptively sample the line projections that are aligned and centered around the edges of the image. Obviously, the image I is unknown and we do not have access to an 'oracle'. As we shall see, this is exactly where the multiresolution nature of the Ridgelet model is useful.

Figure 3.2 show a flow chart of the Adaptive Tomography Acquisition (ATA) algorithm:

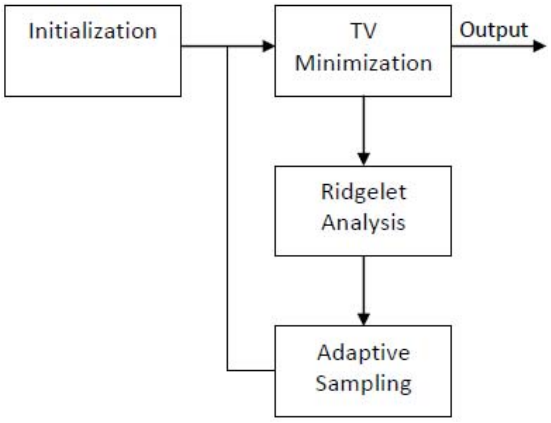

Figure 3.2: Flow chart of the main steps in the ATA algorithm.

Next, a detailed description of the main steps of the ATA algorithm is given:

1. Initialization: We create an initial sampling matrix A using a relatively small uniform set of line projections and sample the image I to obtain an initial observations vector y. The number of the initial line projections is determined relative to the image size. For example, for an image of size 256×256, we measured 8 equally spaced line integrals at eight uniformly spaced angles, which generates a total of 64 initial measurements that are about 0.1% of the image size. Figure 3.4(a) illustrates this non-adaptive uniform sampling pattern for an image of size 256×256. We also initialize the current iteration counter k to 0 and the initial approximation to I, $U^{(-1)}$ to 0.

2. TV Minimization: The inputs to this step are: an updated sampling matrix A (with new additional rows that correspond to the newly acquired line projections) , an observations vector y and the previous approximation $U^{(k-1)}$ as the initial guess. Then, we apply TV minimization step (2.1) or (2.2) (depend on expected noise levels) to compute $U^{(k)}$. Recall, that in our setup, the sparse nature of A enables to process large-scale images.

We have an option to select a tradeoff between reconstruction quality and performance. We do not necessarily need to completely solve the TV minimization problem by iterating the TV solver until it converges as in [12]. Instead, we apply only a fixed and limited number of iterations of the TV solver, or terminate the iterations using a less demanding stopping criterion and proceed to the next step. This speeds up this step in the algorithm, but in some cases, its effect on the next analysis step implies that more line projections are needed to be acquired in order to achieve the same reconstruction quality.

In any case, our adaptive acquisition process terminates if one of the following conditions: $\left\|U^{(k)}-U^{(k-1)}\right\|_2\le\varepsilon$ or number of rows in $A\ge L$, holds, where ε is a predetermined threshold and L is a limit on the total number of line projections that is permitted to be acquired.

3. Ridgelet Analysis: The inputs to this step is an improved approximation $U^{(k)}$ to I. We compute a subset of $U^{(k)}$ Ridgelet coefficients by the application of Radon transform followed by the application of wavelet transform, as shown in (2.4). Since in our application we only use Ridgelets for analysis, we do not need to use the inverse Ridgelet transform as in [16] and that simplifies the implementation. In practice, we realize that if we choose the number of angles to be a quarter of the image length, then our sampling scheme is sufficiently dense for high quality reconstruction, but not too much as to lead to subsequent unnecessary acquisition. Thus, for an images of size 256×256, we compute the Ridgelet coefficients for only 64 uniformly spaced angles, $\theta\in\{0,\pi/64,...,63\pi/64\}$, with 256 line projections per angle. For our experimental results, we applied the univariate discrete Haar wavelet [15] transform at each of the 64 angles to the 256 computed line projections. Then we subsampled the coefficients to avoid unnecessary subsequent acquisition. Specifically, we compute the Ridgelet coefficients $\alpha^{(k)}_{a,b,\theta}(x)\triangleq\left\langle U^{(k)},\psi_{a,b,\theta}\right\rangle$ using the Haar wavelet function $\psi_{a,b}(x)$, in 4 different resolutions, where $a=2^j$, $j=0,...,J_\theta$ and $J_\theta\in\{0,1,2,3\}$ depends on the angle θ. In this case, the discrete sampling of Ridgelet coefficients is controlled by the pairs $(\theta, J_\theta)\in\{(8l\pi/64,3),((8l+1)\pi/64,0),((8l+2)\pi/64,1),((8l+3)\pi/64,0),((8l+4)\pi/64,2),((8l+5)\pi/64,0),((8l+6)\pi/64,1),((8l+7)\pi/64,0)\}$ where, $0\le l<8$.

4. Adaptive Sampling of New Line Projections: The analysis of the Ridgelet coefficients $\alpha^{(k)}_{a,b,\theta}$, computed at step 3, enables us to decide who are the new line projections that are added to A as new rows. Specifically,

we choose these line projections to be associated with the M largest Ridgelet coefficients that have not yet been marked as sampled by the algorithm. The goal of the selected line projections is to approximate (2.3) where ψ is the Haar wavelet. In our experiments, we select $M = 0.1n$, where n is the image row size. In Figure 3.3, we see an illustration of the support of the Haar Ridgelet function (dashed lines) and the associated two line projections (inner lines) within its support. Then, we sample the image I by the updated matrix A to obtain an updated observations vector y.

Now, we look closer at the implication of using only two line projections to approximate the value of the Haar Ridgelet. Assume that the Ridgelet coefficient $\alpha^{(k)}_{a,b,\theta}(x)$ has not been marked as sampled yet but it is significant enough to be sampled at the current iteration. Let $R_I(\theta,\cdot)$ be the Radon transform of the unknown image I at a fixed angle θ. In this case, the two values of the line projections that we acquire are $R_I(\theta, b+a/4)$ and $R_I(\theta, b+3a/4)$. These values are considered as the approximation: $a^{-1/2}\left(R_I(\theta,b+a/4)-R_I(\theta,b+3a/4)\right) \approx CRT_I(a,b,\theta)$.

Hence, the ATA algorithm can be summarized as follows:

ATA $(A, I, M, L, \varepsilon)$

Input: *A - Initial sampling matrix, I - Input image, M - Number of the Ridgelet coefficients subset considered in each iteration. L - Total number of line projections. ε - Stopping threshold.*

Output: *U - Reconstructed image.*

Notations: *u - 1D vector representation of U, A(I) – Sampled image I using the sampling matrix A.*

1. $U^{(-1)} \leftarrow 0.\ k \leftarrow 0.\ \delta \leftarrow 2\varepsilon$

2. While $\delta > \varepsilon$ **and** number of rows in $A < L$

- **2.1.** $y \leftarrow A(I)$
- **2.2.** *Obtain $u^{(k)}$ by solving problem (2.1) or (2.2), using A, y and $U^{(k-1)}$ as the initial guess.*
- **2.3.** *Compute the discrete Ridgelet coefficients of $U^{(k)}$.*
- **2.4.** *Find the M Ridgelet coefficients that have the largest absolute values that have not been sampled yet.*
- **2.5.** *For each of the newly found Ridgelet coefficients: add new rows to A associated with line projections, whose sampling approximates the value of the Ridgelet coefficient on the image I.*
- **2.6.** $\delta \leftarrow \left|u^{(k)} - u^{(k-1)}\right|.\ k \leftarrow k+1.$

3. Return $U^{(k-1)}$.

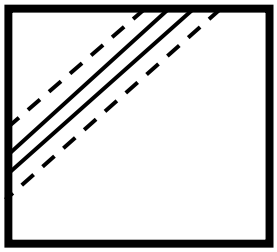

Figure 3.3: Line integrals that were acquired per a significant Ridgelet coefficient: The external dashed lines correspond to the support of the Ridgelet and the inner lines are the sampled line projections

In Figure 3.4, we see the output from 4 iterations of the ATA algorithm on the 'Ellipse' image (shown in Fig. 3.4 (h)). Figs. 3.4 (a) and (b) show the uniform acquisition pattern described in the initialization step and the resulted first approximation image $U^{(0)}$, respectively. Figs. 3.4 (c), (e) and (g) show the newly sampled line projections associated with the next M largest unsampled Ridgelet coefficients in iterations 0,1 and 2. Figs 3.4 (d), (f) and (h) show the resulted approximation images $U^{(k+1)}$ ($k = 0,1,2.$) produced by solving (2.1) after updating A with the new corresponding rows. We see that the algorithm quickly identifies the edges of the ellipse and only samples around them with more samples along the longer axis first. Moreover, initially, when the approximation $U^{(k+1)}$ is still blurred (Fig. 3.4 (b)), the algorithm finds from the Ridgelet analysis that it should first acquire line projections associated with Ridgelet coefficients from coarse resolution as seen in Figs. 3.4 (c) and (e). Only after the approximation contains sufficiently sharp edges (Fig. 3.4 (f)), Ridgelet coefficients from finer resolution become significant and the line projections associated with them are acquired as seen in Fig. 3.5 (g). In summary, the ATA algorithm attempts to acquire only line projections that are around and aligned with edge singularities that are ordered by resolution.

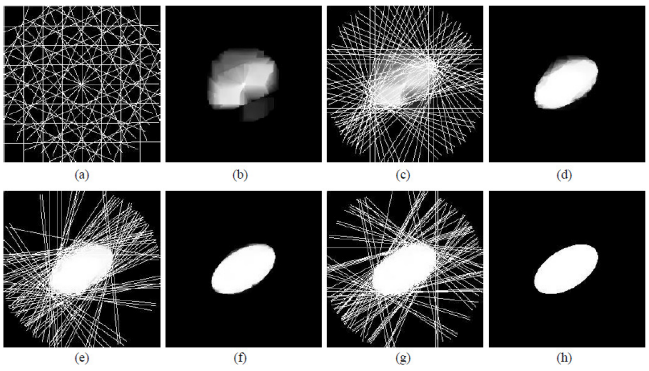

Figure 3.4: Adaptive acquisition of the Ellipse image: Iterations of newly added projection lines and approximations $U^{(k)}$.

4. Experimental Results

In this section we compare the ATA algorithm with known limited angle (non-adaptive) methods and also examine the quality of the estimate for the significant Ridgelet coefficients of the image I produced by our algorithm. We show that for a given number of line projections measured on the image I, ATA produces a significantly better approximation to I. The experiments were conducted on 256×256 well known phantom test images: 'Shepp Logan' and 'Zubal head' [18] in 2 different setups: noisy and noise free. We use the standard Peak Signal to Noise Ratio (PSNR), measured in dB, to quantify an approximation U to the image I where the image pixels take values in [0,1], $PSNR(I,U)\triangleq 10\log_{10}\left((N^{-1}\sum_{i,j}\left|I_{i,j}-U_{i,j}\right|^2)^{-1}\right)$. Given an $m\times m$ image, we prescribe a target of n samples. Denote $d=n/m$ (assuming $n \bmod m=0$). We compare five acquisition and reconstruction methods:

1. Filtered Back Projection (FBP): For the FBP method we sampled $60\times m$ line projections (regardless of the target limit), which are m equally spaced line integrals over the angles $0,\pi/60,...,59\pi/60$. We then used the MATLAB implementation ('iradon') to obtain a reconstructed image.

2. Non Adaptive Equally Spaced (NAS): We used equally spaced rotations and a fixed number of line projections at each angle such that the total number of line projections matched the prescribed budget. We then applied TV minimization to this sampled data. Specifically, $m/2$ (equally spaced) line projections were acquired over the angles $0,\pi/2d,2\pi/2d,...,(2d-1)\pi/2d$.

3. Non Adaptive Uniform Fourier (NAF): This method is used in [22]. In this mode, we uniformly select lines in the Fourier domain of the image and use Fourier coefficients on these lines as the entries of the sampling matrix A. Specifically, m Fourier coefficients were taken on the lines associated with the angles $0,\pi/d,2\pi/d,...,(d-1)\pi/d$.

4. Adaptive Tomography Acquisition (ATA): Our proposed adaptive algorithm (see Section 3).

5. ATA using an oracle (ATA oracle): The same algorithm used in 4, but now we allow ATA to use the Ridgelet analysis of the I instead of using the Ridgelet analysis performed on the iterated approximated image.

The first tests are noise free. In these tests we solve the problem (2.1). In Figs 4.1, 4.2 we see that the ATA algorithm achieves perfect reconstruction using the smallest number of line projections, while the uniform limited angle, non-adaptive acquisition algorithms (NAS and NAF, that equipped with the same TV minimization solver and FBP) achieve significantly lower image quality. Figure 4.3 shows a comparison between PSNR values of methods 2-5 for different numbers of line projections for the 'Shepp-Logan' image. We see, that despite of not having the image I available at the time of acquisition, our algorithm manages to perform almost as good as an algorithm equipped with an 'oracle' that uses the Ridgelet analysis of the image I.

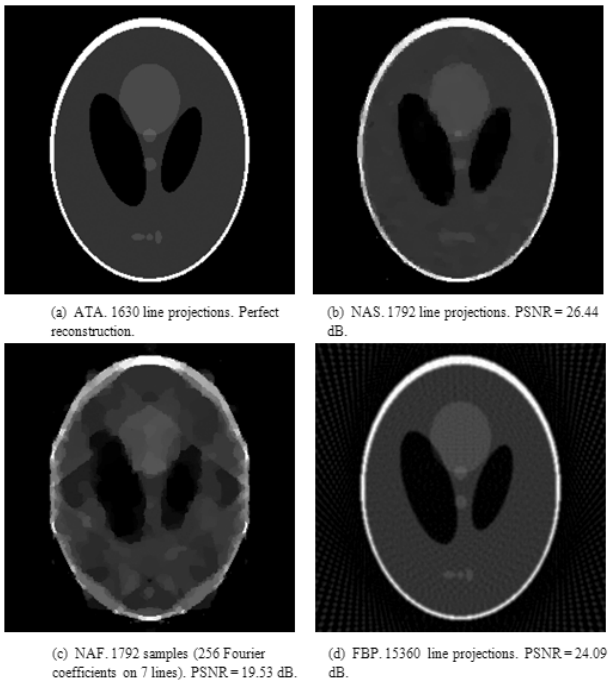

(a) ATA. 1630 line projections. Perfect reconstruction.

(b) NAS. 1792 line projections. PSNR = 26.44 dB.

(c) NAF. 1792 samples (256 Fourier coefficients on 7 lines). PSNR = 19.53 dB.

(d) FBP. 15360 line projections. PSNR = 24.09 dB.

Figure 4.1: PSNR comparison between non-adaptive and adaptive acquisition methods for the reconstruction of the 'Shepp-Logan' image.

Next, we show results with simulated low dose as in [3]. For a selected parameter of incident photon count γ_I, the simulated detected photon counts $\tilde{\gamma}$, were chosen as Poisson distributed random variables with mean equal to $\gamma_I e^{-p}$, where p is a noiseless line projection. The simulated noisy projection, $\tilde{p}$, is then determined by $\tilde{p}=-\log\left(\tilde{\gamma}/\gamma_I\right)$. This time, in our iterations, we solve the problem (2.2), which provides better regularity for noisy data. In Figure 4.4 we see a comparison of ATA and NAS using dose simulation for the Shepp-Logan image. We see that the image quality produced by ATA is higher for a smaller number of line projections. Figure 4.5 shows a clear advantage of ATA over the compared methods on the 'Zubal Head' image under a dose simulation. In Figure 4.6, we see a plot of PSNR reconstruction values at various simulated dose levels for the Shepp Logan image.

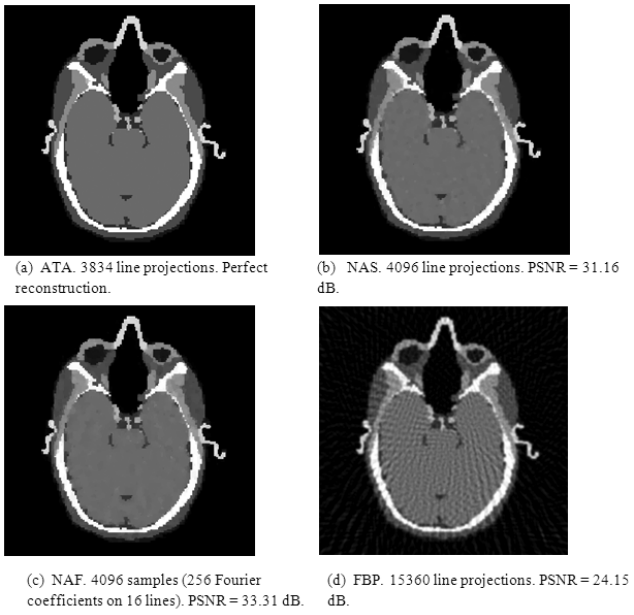

(a) ATA. 3834 line projections. Perfect reconstruction.

(b) NAS. 4096 line projections. PSNR = 31.16 dB.

(c) NAF. 4096 samples (256 Fourier coefficients on 16 lines). PSNR = 33.31 dB.

(d) FBP. 15360 line projections. PSNR = 24.15 dB.

Figure 4.2: PSNR comparison between non-adaptive and adaptive acquisition methods for the reconstruction of the 'Zubal-head' image.

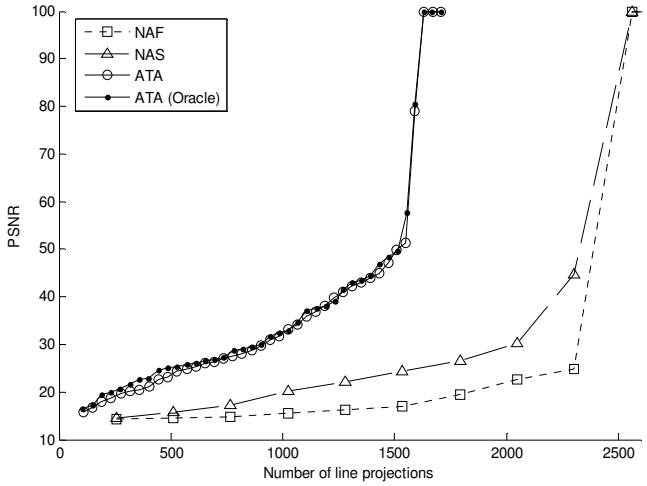

Figure 4.3: PSNR comparison between the ATA algorithm, ATA with an oracle and the non-adaptive methods of NAS and NAF after their applications to the 'Shepp-Logan' image.

We note that currently the running times of the ATA algorithm, simulated on Matlab, are about 7-10 slower than the non-adaptive methods (NAS, NAF) for the same number of line projections. This relates to the choice of M, the number of new line projections introduced at each iteration. For a given number of line projections L, the choice $M = 0.1L$ yields about 10 iterations, where the

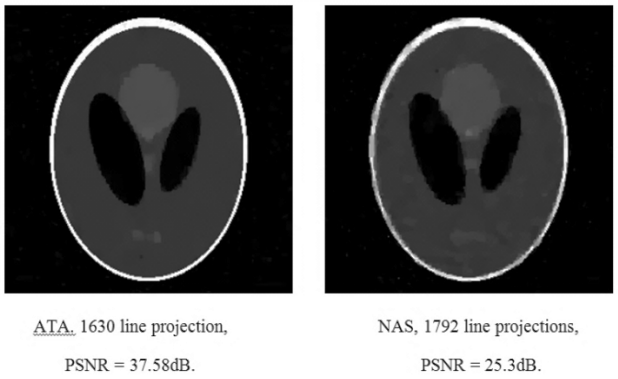

ATA. 1630 line projection, PSNR = 37.58dB.

NAS, 1792 line projections, PSNR = 25.3dB.

Figure 4.4: PSNR comparison between ATA and NAS for the reconstruction of the 'Shepp-Logan' image at simulated incident photon count $\gamma_I = 250000$.

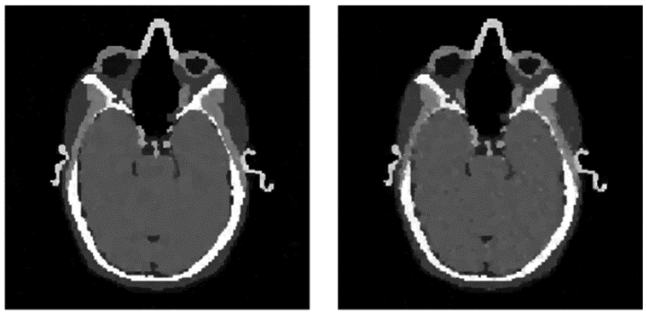

ATA. 3834 line projections, PSNR = 33.44 dB.

NAS. 4096 line projections, PSNR = 29.26 dB.

Figure 4.5: PSNR comparison between ATA and NAS for the reconstruction of the 'Zubal-head' image at simulated incident photon count $\gamma_I = 1000000$

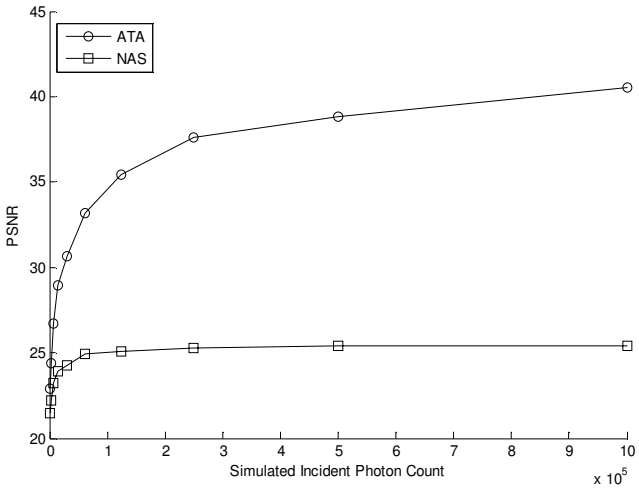

Figure 4.6: PSNR comparison between the ATA algorithm and NAS after their application to the 'Shepp-Logan' image for various simulated incident photon counts .

matrix A, in the kth iteration ($k = 1,\ldots,10$), contains about $0.1kL$ rows. Solving these iterations is about 5.5 slower than solving the TV-minimization of order n only once. The rest of the running time of ATA is spent on the Ridgelet analysis computations that are performed at each iteration.

5. Conclusion and Future Work

In this paper we propose a mathematical model for adaptive CT acquisition whose theoretical goal is to radically reduce dosage levels, while maintaining high quality reconstruction. We presented numerical simulations that demonstrate the potential of the mathematical model of adaptive acquisition and compared our results to known limited angle, non adaptive acquisition methods.

Our future research will focus on creating more realistic simulations of CT acquisition. We plan to enhance our algorithm to perform well on more realistic images and model more accurately adaptive low-dose radiation, beyond the simplistic model of the total number of line projections (dose in a CT scan depends on the machine's flux intensity, with lower flux intensity implying lower dose, but higher Poisson-type noise in the detected measurements). We also plan to simulate true 3D scanning and add motion correction.

Lastly, as discussed in Section 4, running time is a drawback of the ATA algorithm. At each iteration, the ATA algorithm updates the sampling matrix A and solves the whole optimization problem again, which is an expensive computational task. We plan to explore an efficient updating scheme that allows the current approximated image to be modified solely by the newly acquired line projections and by the previous approximated image. This efficient scheme will eliminate the need to solve the whole problem from the beginning. Furthermore, it should be interesting to test other TV solvers such as [19] and see if they (or a modified version of them) are better suited to the adaptive scheme proposed in this paper.

References

[1] D. Brenner, C. Ellison, E. Hall and W. Berdon, Estimated risks of radiation-induced fatal cancer from Pediatric CT. American Journal of Roentgenology 176 (2001), 289-296.

[2] C. McCollough, M. Bruesewitz and J. Kofler, CT Dose Reduction and Dose Management Tools: Overview of Available Options, Radiographics 26 (2006), 503-512.

[3] A. Delaney and Y. Bresler, Globally Convergent Edge-Preserving Regularized Reconstruction: An Application to Limited-Angle Tomography, IEEE Trans. Image Proc. 7 (1998), 204-221.

[4] J. Thibault, K. Sauer, C. Bouman and J. Hsieh, A three-dimensional statistical approach to improved image quality for multislice helical CT, Med. Phys. 34 (2007), 4526-4544.

[5] E. Candès, Ridgelets: Theory and applications, Ph.D. Thesis, Stanford University, 1998.

[6] "MBIR aims to outshine ASIR for sharpness, CT dose reduction", article in AuntMinnie, 18th May, 2010.

[7] D. Kolditz, Y. Kyriakou and W. Kalender, Volume-of-interest (VOI) imaging in C-arm flat-detector CT for high image quality at reduced dose, Medical Physics 37 (2010), 2719-2730.

[8] J. Moore, H. Barret and L. Furenlid, Adaptive CT for high-resolution, controlled-dose, region-of-interest imaging, IEEE Nucl. Sci. Symp Conf. (2009), 4154-4157.

[9] B. Rutt, Scanned projection radiography using high speed computed tomographic scanning system, U.S Patent 4,573,179.

[10] T. Quinto, Singularities of the X-ray transform and limited data tomography in $\mathbb{R}^2$ and $\mathbb{R}^3$, SIAM J. Math. Anal., 24(1993), 1215-1225.

[11] Compressive Sensing Resources home page: http://dsp.rice.edu/cs .

[12] C.Li, Compressive Sensing for 3D Data Processing Tasks: Applications, Models and Algorithms, Ph.D. thesis, Rice University, April 2011.

[13] TVAL3 homepage : http://www.caam.rice.edu/~optimization/L1/TVAL3/

[14] B. De Man and S. Basu. Distance-driven projection and backprojection in three dimensions. Phys. Med. Biol., 49 (2004), 2463-75.

[15] S.Mallat, A Wavelet Tour of Signal Processing, Third Edition: The Sparse Way, 3rd edition, Academic Press, 2009.

[16] M. N. Do and M. Vetterli, The Finite Ridgelet transform for image representation, IEEE Trans. Image Proc. 12 (2003), 16-28.

[17] J.Hsieh, Computed Tomography, principles, design, artifacts and recent advances, second edition, 2009.

[18] I. Zubal, C. Harrell, E. Smith, Z. Rattner, G. Gindi, and P. Hoffer, Computerized three-dimensional segmented human anatomy, Med. Phys. 21(1994), 299-302.

[19] Y.Mao, B.P. Fahimian, S. J. Osher, and J. Miao, Development and optimization of regularized tomographic reconstruction algorithms, IEEE Trans. Image Proc. 19 (2010), 1259-1268.

[20] R. Nelson, Thousands of new cancers predicted due to increased use of CT, Medscape news, December 17, 2009.

[21] I. Shuryak, R. Sachs and D. Brenner, Cancer Risks after Radiation Exposure in Middle Age, Journal of the National Cancer Institute 102 (2010), 1606-1609.

[22] E. Candes, J. Romberg, and T. Tao, "Robust uncertainty principles: Exact signal reconstruction from highly incomplete frequency information," IEEE Trans. Inf. Theory, vol. 52, no. 2, pp. 489–509, 2006.

[23] J. Frikel, A new framework for sparse regularization in limited angle x-ray tomography, Proc. IEEE conf. biomedical imaging 2010, 824-827.